PNAS

Supporting Information for

Surface Coating by Mechanofusion Modulates Bulk Charging Pathways and Battery Performance of Ni-rich Layered Cathodes

Dong Hou, Jiaxiu Han, Chenxi Geng, Zhengrui Xu, Modhi M AlMarzooqi, Jin Zhang, Zhijie Yang, Jungki Min, Xianghui Xiao, Olaf Borkiewicz, Kamila Wiaderek, Yijin Liu, Kejie Zhao, and Feng Lin

Corresponding authors: Feng Lin, and Kejie Zhao
Email: fenglin@vt.edu, kjzhao@purdue.edu

This PDF file includes:

Other supporting materials for this manuscript include the following:

Supporting Information Text

Note S1, details of XANES-3DTXM measurements and data processing

X-ray tomography measurement can be achieved by taking TXM projections of a rotating sample at each fraction of a degree. The 2D images collected at all angles are then reconstructed into a 3D volume. The hard X-rays can penetrate through the sample, enabling non-destructive 3D analysis of structure and morphology within the sample. A more powerful technique is coupling TXM with X-ray absorption near edge structure (XANES) spectroscopic capability. This is achieved by collecting and reconstructing TXM projections at a series of X-ray energies across the absorption edge of an element. A XANES spectrum can be generated at each voxel of the reconstructed 3D volume by imposing and aligning the absorption objects at different energies, which involves sophisticated image alignment in the data processing. The shape of the XANES spectra represents the local chemical fingerprints of the element, therefore the 3D information on oxidation states can be achieved by fitting the spectrum on every voxel of the object. 2DTXM is a projection through the entire sample, the depth profile along the beam direction is not available. A great advantage of XANES-3DTXM is the 3D structure from X-ray tomography and XANES imaging can offer great capability for finer chemical and morphological features inside the sample.

In order to do quantification and further analysis of the morphological characteristics, the greyscale absorption mapping is normalized and then binarized using Otsu's thresholding method, which is effective on minimizing the intraclass variance of the black and white pixels after binarization.(1)

Note S2, details of SXRD peak fitting and refinements

Peak fitting on selected reflections was performed using MATLAB. Pseudo-Voigt peak-shape functions with polynomial function for background were applied in the least-squares fitting routine. The Le Bail fit for *in situ* SXRD patterns were conducted in GSAS-II,(2, 3) the background terms, unit cell parameters, and peak profiles were refined. For Rietveld analysis of *ex situ* powder SXRD, the scale factor, zero offset, atomic positions, occupancies, and atomic displacement parameters were also refined. The instrument parameters were calibrated by refining a standard CeO_2 for APS datasets or Ni for NSLS-II datasets.

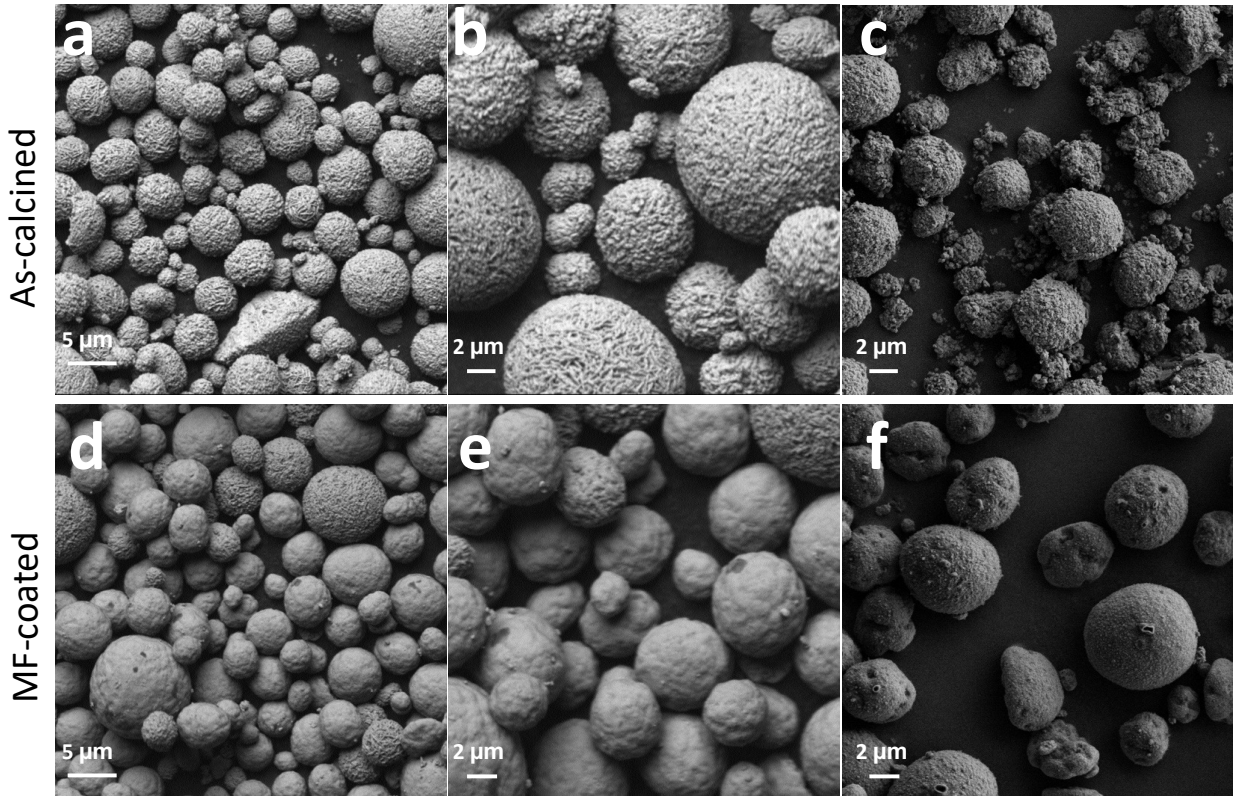

Fig. S1. SEM images of NMC secondary particles for (a-c) as-calcined and (d-f) MF-coated NMC powders

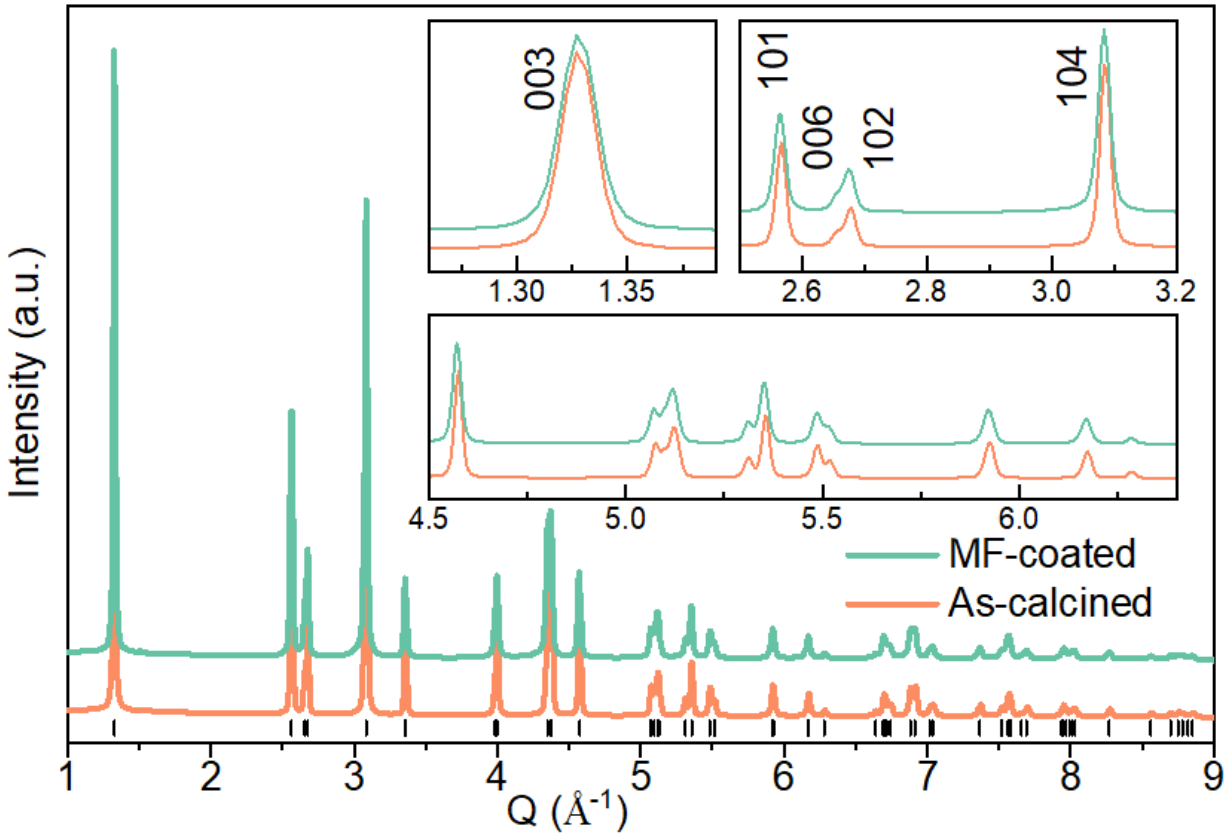

Fig. S2. Comparison of SXRD patterns between as-calcined and MF-coated NMC powders. The reflections were marked in a $R\bar{3}m$ structure, and representative reflections were annotated with miller indices in the subplots.

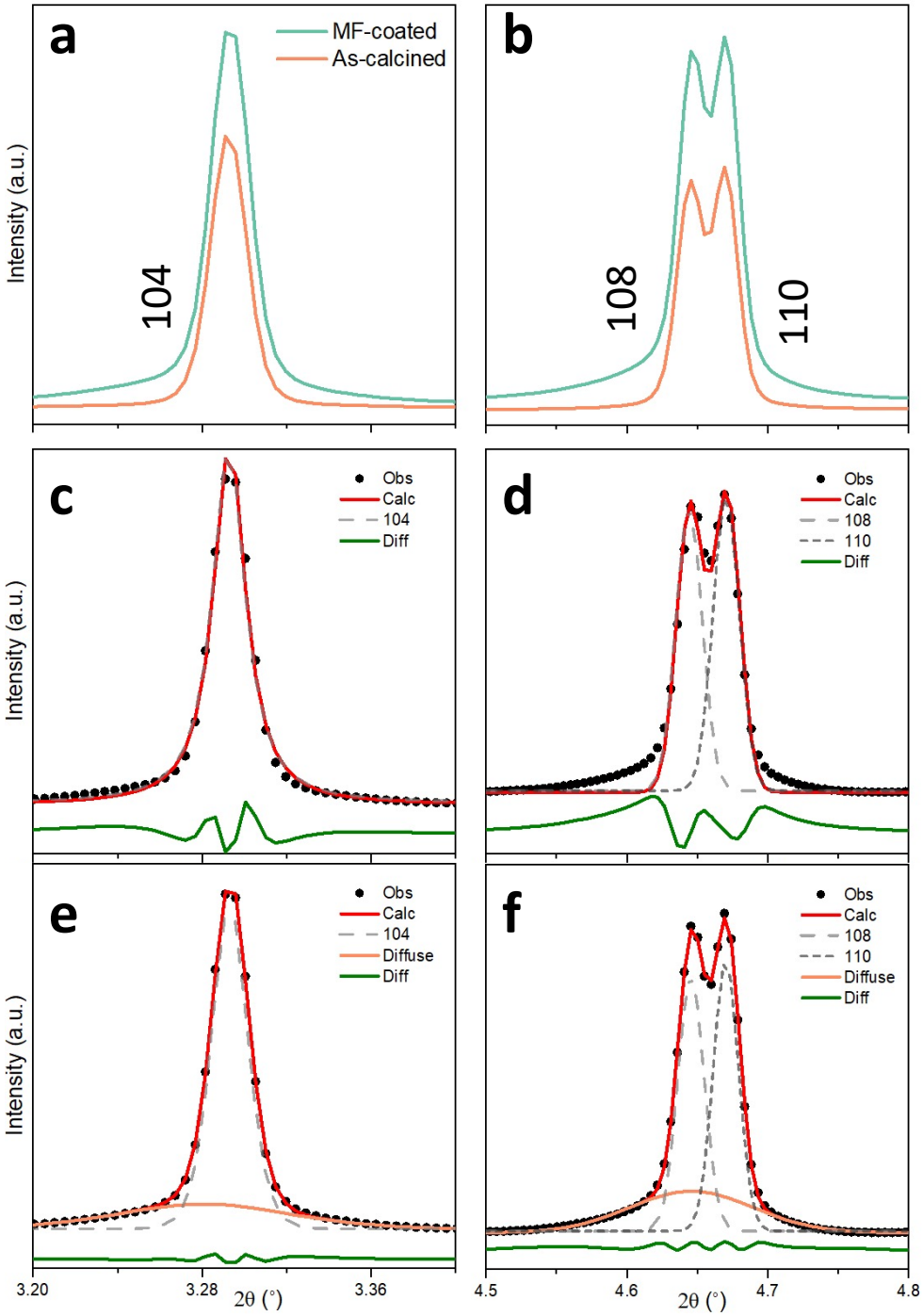

Fig. S3. Selected reflections and the peak fittings. (a) 104 reflection for as-calcined and MF-coated NMCs. (b) 108 and 110 doublets for both NMCs. (c, d) Fitting of each reflection on MF-coated pattern using single Pseudo-Voigt function. (e, f) Fitting of the same reflection by introducing a diffuse peak, demonstrating the existence of non-uniform lattice strain after MF-coating.

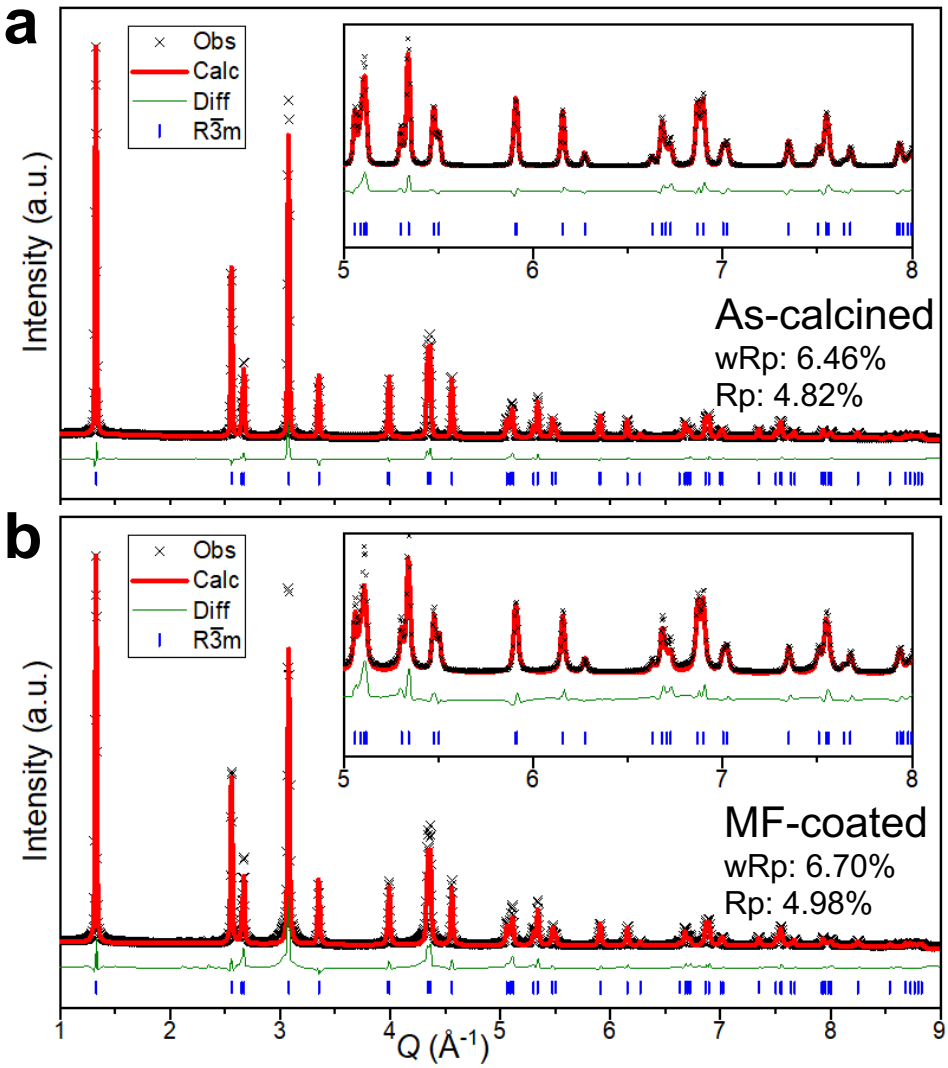

Fig. S4. Representative refinements for pristine (a) as-calcined and (b) MF-coated NMCs using a single *R*$\bar{3}$*m* model.

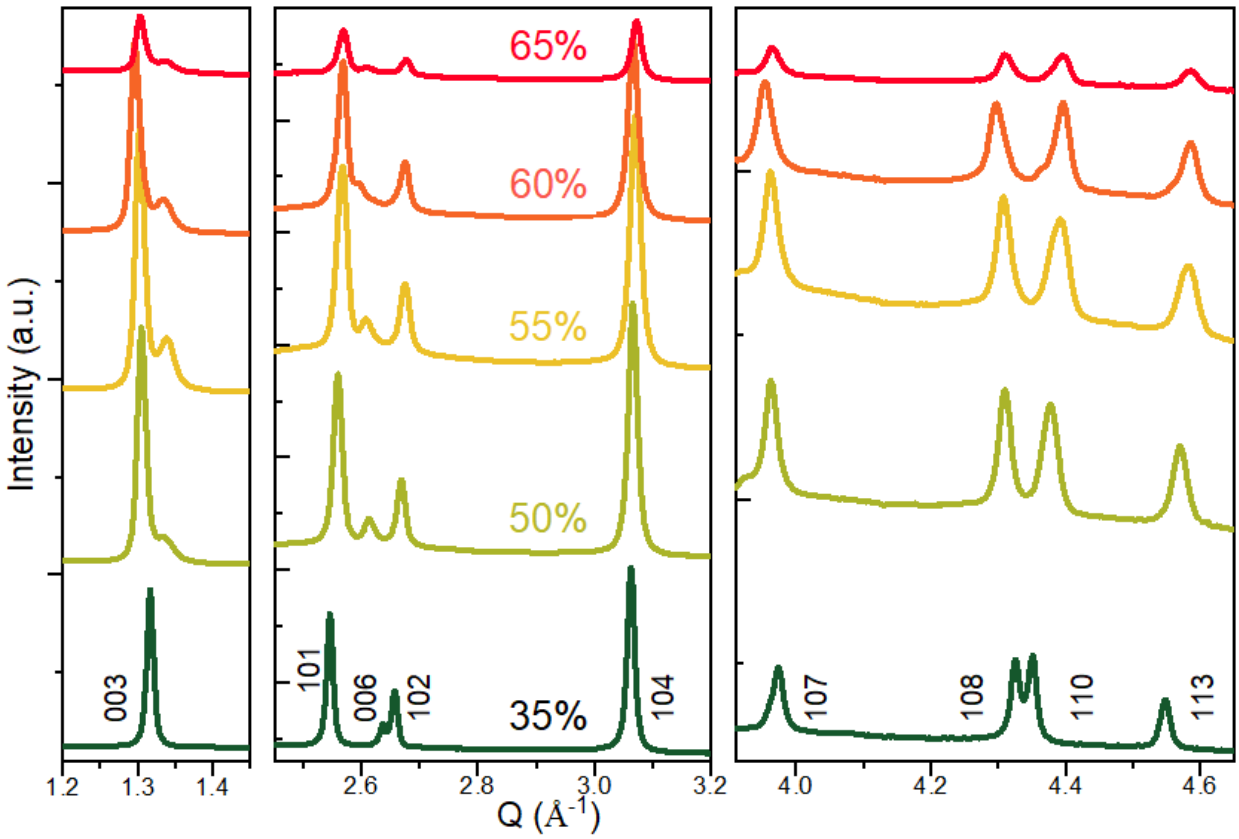

Fig. S5. Synchrotron XRD patterns of MF-coated NMCs as a function of chemically delithiation levels.

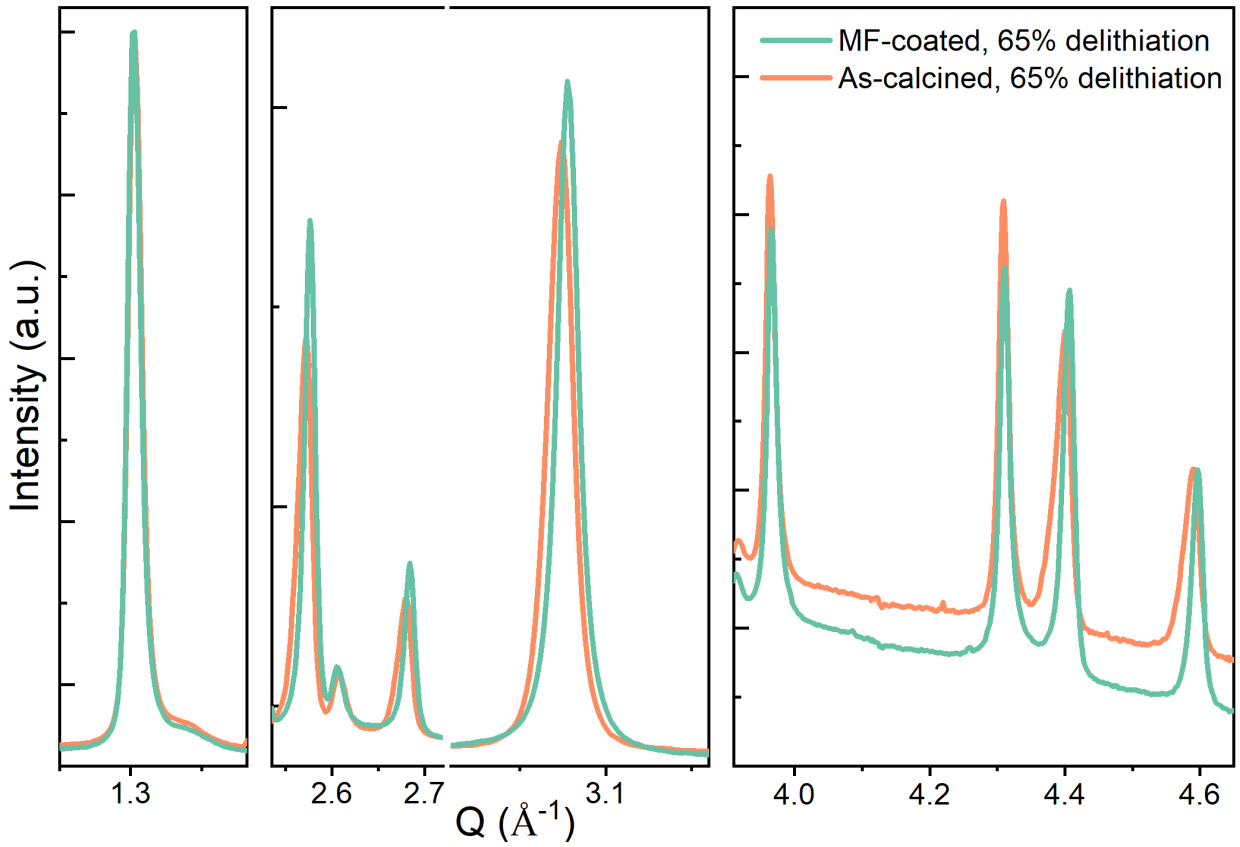

Fig. S6. Comparison of SXRD patterns between as-calcined and MF-coated NMC powders after deep (~65%) delithiation. The MF-coated NMC show less peak shift and broadening comparing to the as-calcined one after delithiation.

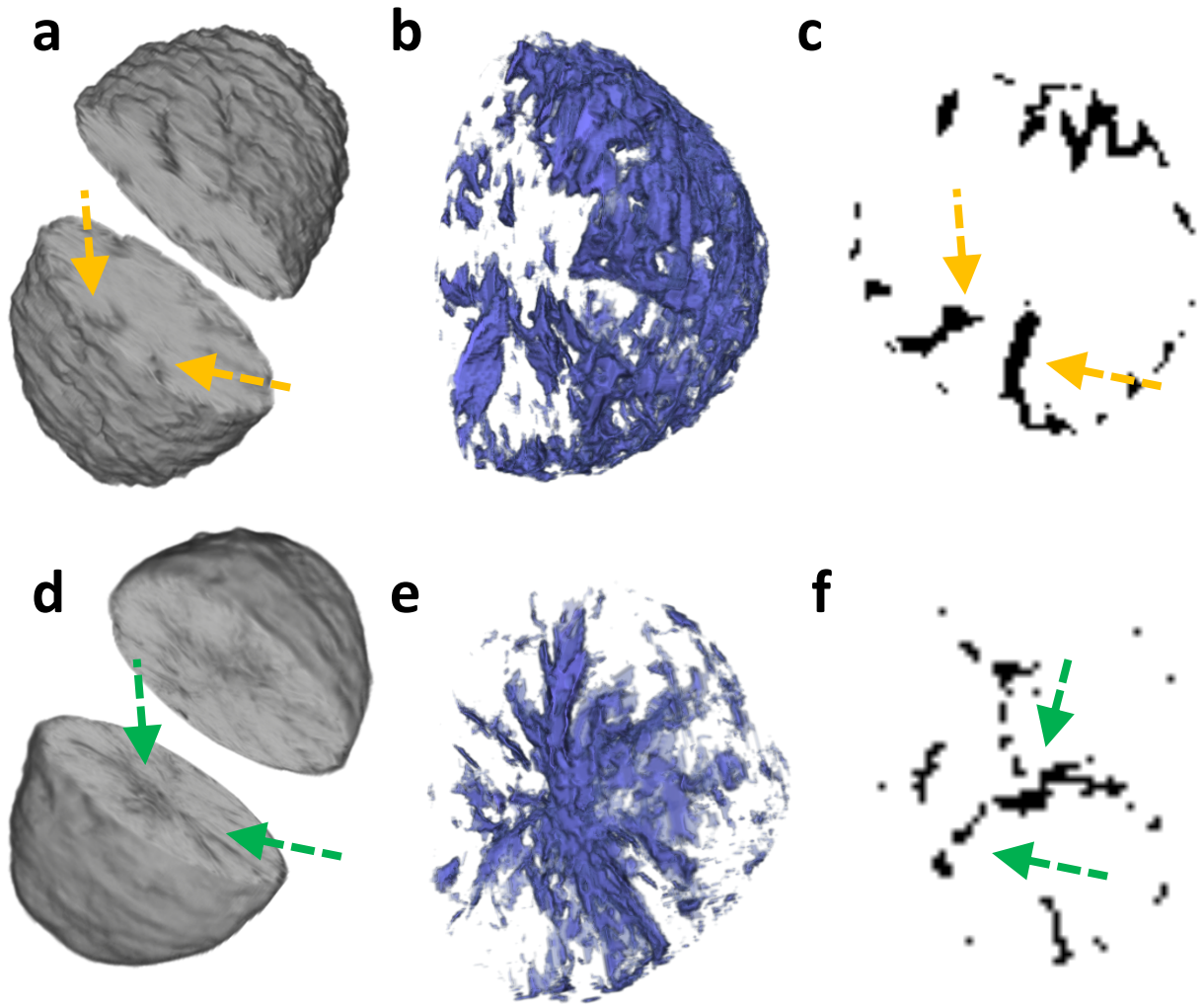

Fig. S7. Rendering of the secondary particle tomography, voids volume, and selected 2D voids slice. (a-c) are for as-calcined NMCs after mild delithiation. (d-f) are the corresponding datasets for MF-coated NMCs. Arrows in yellow indicate the cracks initiated from surface for as-calcined NMCs, while arrows in green are for radial cracks generated under delithiation for MF-coated NMCs. Note the illustrations are not drawn to scale for the demonstration purpose.

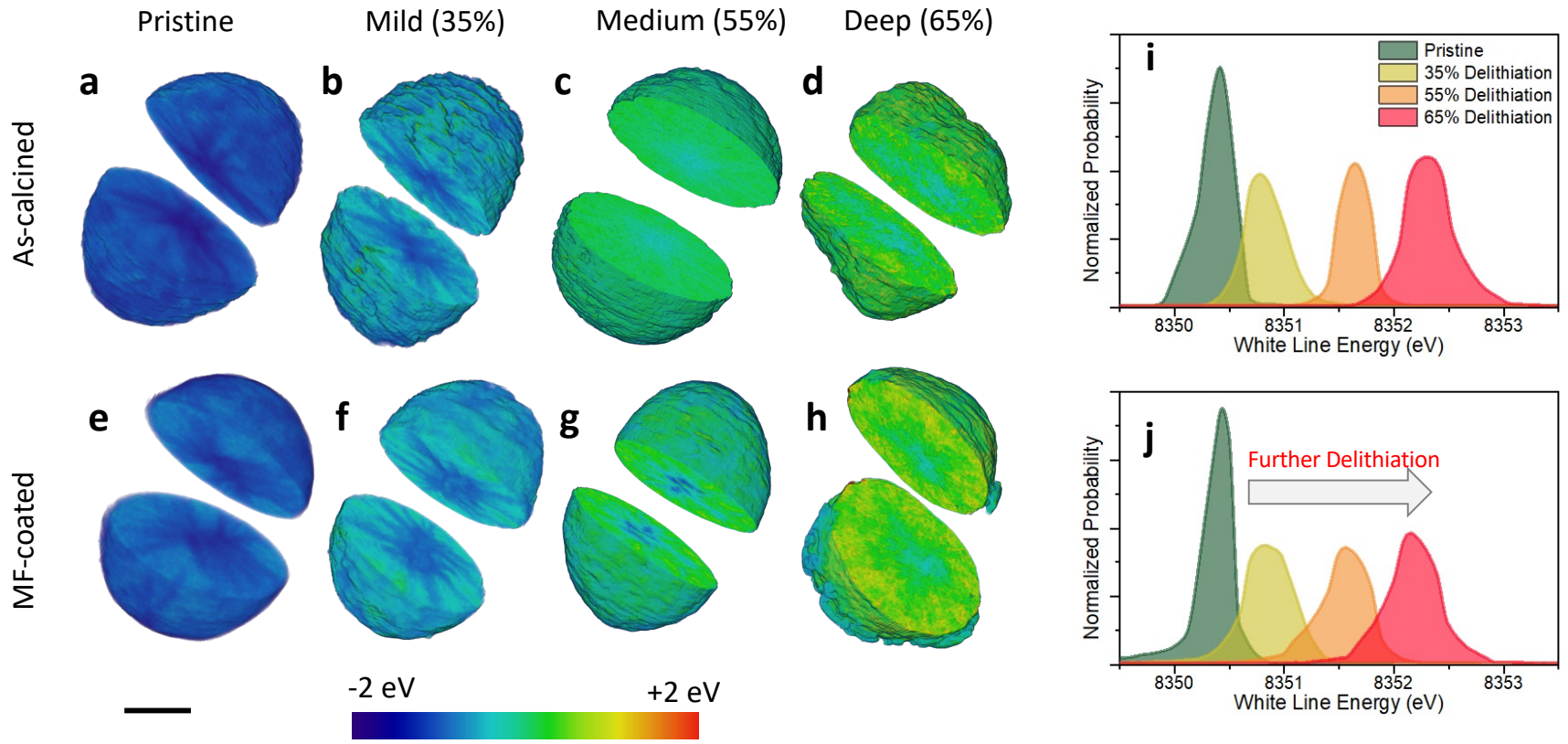

Fig. S8. State of charge distribution for NMC particles as a function of delithiation from XANES-3DTXM. (a-d) *Ex situ* 3D rendering of Ni white-line energy distribution for as-calcined NMCs under different delithiation, with a scale bar of 5 μm. The same set of plots for MF-coated particles are shown in (e-h). The histogram of white-line energies at each delithiation level for (i) as-calcined and (j) MF-coated NMCs.

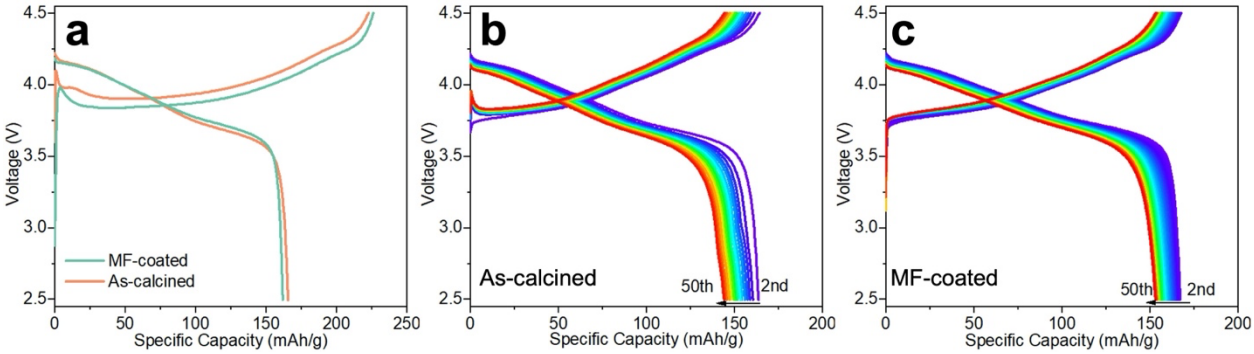

Fig. S9. (a) Initial charge to 4.5 V and then discharge to 2.5 V versus Li/Li$^+$ at 1C for as-calcined and MF-coated NMC half cells. Cycling profiles for (b) as-calcined and (c) MF-coated NMC cells. The low mass loading electrodes are used to eliminate the electrode internal polarization to better reflect the intrinsic degradation of the active particles. The cells were all tested at 22 °C and 1C. 1 C was defined as fully charging the cathode in 1 h, with a specific capacity of 200 mAh g^{-1}.

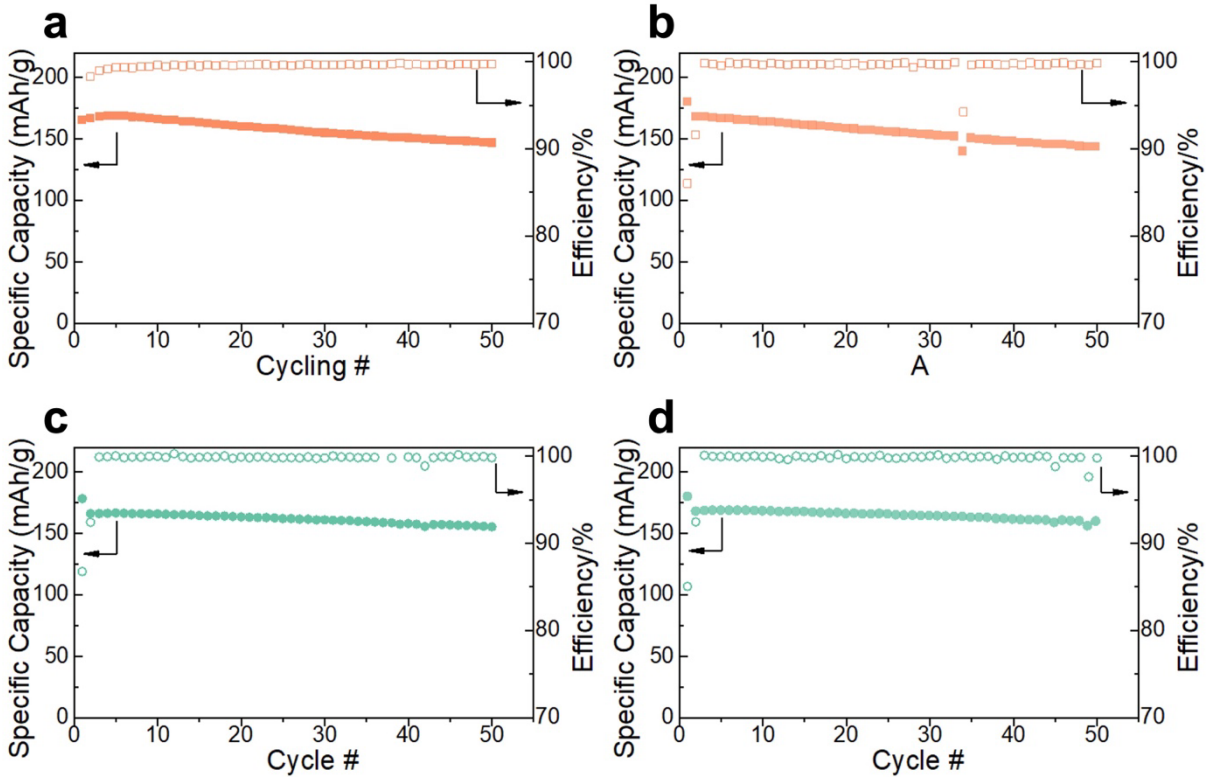

Fig. S10. (a-b) Replicate of the cycling performance of as-calcined NMCs. The average capacity is 166.2 ± 1.6 mAh g^{-1}. (c-d) Replicate of the cycling performance of MF-coated NMCs. The average capacity is 167.1 ± 1.3 mAh g^{-1}. The cells were all tested at 22 °C and 1C. 1 C was defined as fully charging the cathode in 1 h, with a specific capacity of 200 mAh g^{-1}.

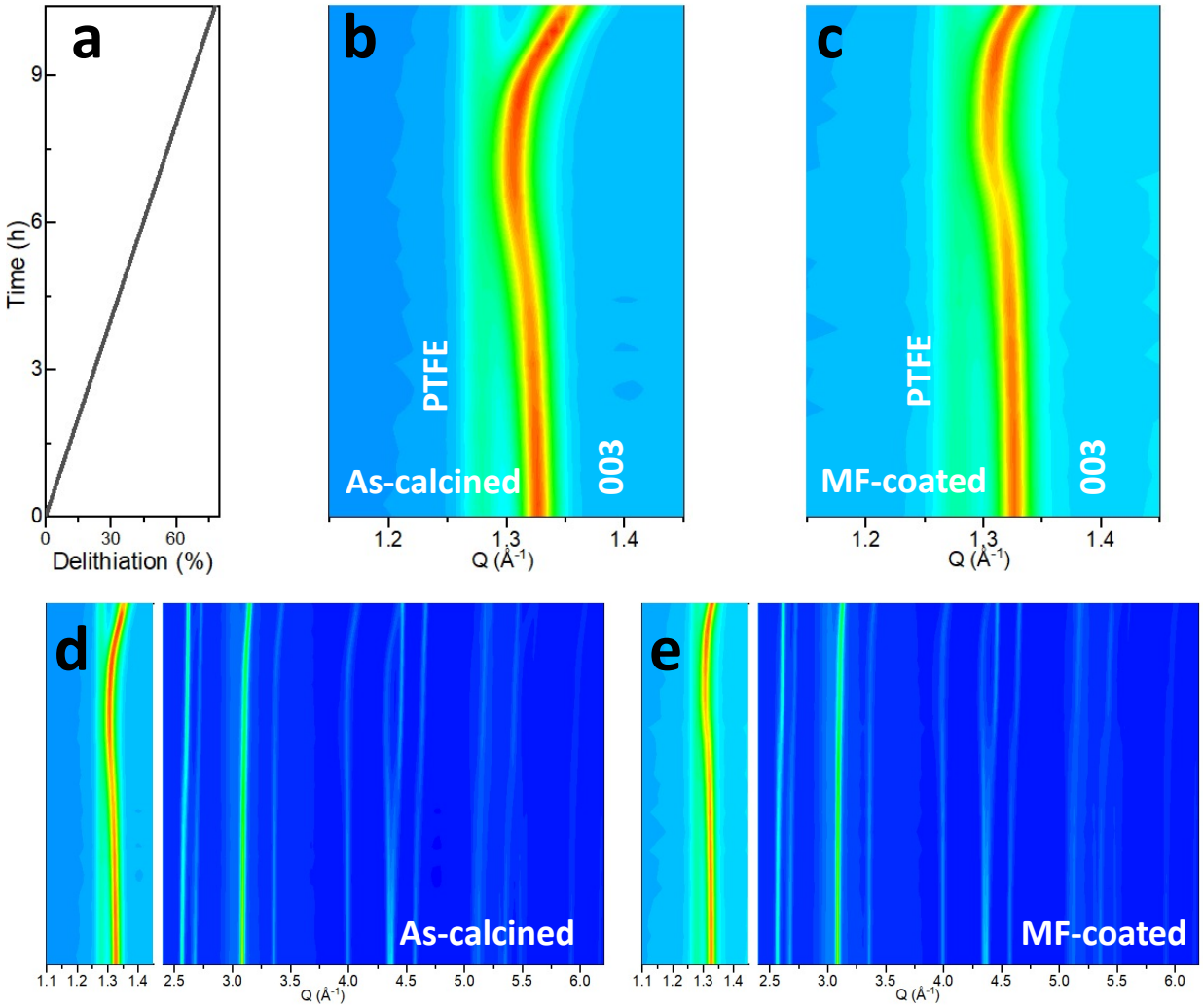

Fig. S11. *in situ* cycling SXRD for as-calcined and MF-coated NMC cells. (a) The delithiation as a function of SXRD collection time. Zoom in view of 003 reflection region for (b) as-calcined and (c) MF-coated NMCs. The signal from PTFE binder was noted. The full *in situ* SXRD patterns for (d) as-calcined and (e) MF-coated NMC cells.

Table S1. Crystallographic information of pristine as-calcined and MF-coated NMCs.

Samples	Lattice Parameters			Relative changes (%)		
	a (Å)	*c* (Å)	Vol (Å^3)	$\triangle a$	$\triangle c$	$\triangle$Vol
As-calcined	2.87183	14.19579	117.07880			
MF-coated	2.87421	14.19591	117.27400	0.083	0.001	0.167

Table S2. Li content and TM ratios from ICP-MS for pristine and delithiated NMCs. The cation ratios were derived by assuming the summation of TM concentration to 1.

Delithiation Levels	Cation Ratios	
	As-calcined	MF-coated
Pristine	$Li_{1.00}Ni_{0.83}Mn_{0.05}Co_{0.12}$	$Li_{1.00}Ni_{0.82}Mn_{0.06}Co_{0.12}$
Mild (~35%)	$Li_{0.63}Ni_{0.83}Mn_{0.05}Co_{0.12}$	$Li_{0.63}Ni_{0.83}Mn_{0.05}Co_{0.12}$
Medium (~55%)	$Li_{0.44}Ni_{0.84}Mn_{0.04}Co_{0.12}$	$Li_{0.44}Ni_{0.83}Mn_{0.05}Co_{0.12}$
Deep (~65%)	$Li_{0.38}Ni_{0.83}Mn_{0.05}Co_{0.12}$	$Li_{0.34}Ni_{0.82}Mn_{0.06}Co_{0.12}$

Table S3. Parameters used in finite element modeling.

Parameter	Symbol	Value
Particle radius	r	5×10^{-6} m
Elastic constants	C_{11}	259 GPa
	C_{12}	107 GPa
	C_{13}	75 GPa
	C_{33}	194 GPa
	C_{44}	59 GPa
Li diffusivity along *ab* plane	D_{ab}	2×10^{-14} m^2/s
Li diffusivity along *c* direction	D_c	2×10^{-15} m^2/s
Li diffusivity in MF coating layer	D_L	2×10^{-14} m^2/s
Maximum Li concentration	C_{max}	63887 mol/m^3
Tensile strength	t_n	200 MPa
Fracture toughness	G_c	2 J/m^2

Movie S1 (separate file). The evolution of the Li concentration and intergranular fracture along the grain boundaries for as-calcined NMC during charging.

Movie S2 (separate file). The evolution of the Li concentration and intergranular fracture along the grain boundaries for MF-coated NMC during charging.

SI References

1. N. Otsu, A Threshold Selection Method from Gray-Level Histograms. *IEEE Trans Syst Man Cybern* **9**, 62–66 (1979).
2. A. le Bail, A. Jouanneaux, A Qualitative Account for Anisotropic Broadening in Whole-Powder-Diffraction-Pattern Fitting by Second-Rank Tensors. *J Appl Crystallogr* **30**, 265–271 (1997).
3. B. H. Toby, R. B. von Dreele, GSAS-II : the genesis of a modern open-source all purpose crystallography software package. *J Appl Crystallogr* **46**, 544–549 (2013).